



Formation of iron oxide and iron sulfide at high temperature and their effects on corrosion

Shujun Gao*, Bruce Brown, David Young, Marc Singer

Institute for Corrosion and Multiphase Technology, Department of Chemical & Biomolecular Engineering, Ohio University, 342 West State Street, Athens, OH, 45701, USA



ARTICLE INFO

Keywords:

Hydrogen sulfide
High temperature corrosion
Iron oxide
Iron sulfide

ABSTRACT

Recent high temperature H₂S corrosion study reported that a thermodynamically less stable iron oxide layer can also form in addition to iron sulfide. In this work, H₂S corrosion experiments were conducted at 120 °C for different exposure times, ranging from 1 to 21 days. The inner layer was identified by Transmission Electron Microscopy (TEM) as Fe₃O₄ (magnetite); Fe₃O₄ was always present over time despite it being less stable than iron sulfide. The observed formation sequence of iron sulfide at high temperature was mackinawite → troilite → pyrrhotite → pyrite. The role of the different corrosion product layers in corrosion is discussed.

1. Introduction

As exploration and drilling conditions for petroleum involve ever higher pressure and temperature (HPHT) in combination with high H₂S content, development of adequate asset integrity management practices (associated with technology development, regulation, and corrosion mitigation) brings many new challenges [1–5]. In 2008, it was reported that at least 11% of wells to be drilled were expected to be at temperatures exceeding 177 °C [1]. HPHT wells are now very common worldwide, from the North Sea and the Gulf of Mexico to Southeast Asia, Africa, and South America [6]. The likelihood of encountering H₂S corrosion also correlates with the increase of temperature in these wells [7]. H₂S corrosion at lower temperatures (< 80 °C) has been extensively studied over the past several decades [8–10], and significant progress has been made related to the understanding of the associated mechanisms. However, research related to H₂S corrosion mechanisms at higher temperatures (> 80 °C) has, so far, been limited. Laboratory experiments at temperature below 80 °C are typically conducted in a glass cell, while autoclaves are used when the temperature is above 80 °C.

In our previous high temperature H₂S corrosion study [11], iron oxide was observed as an inner corrosion product layer. A thin layer (~5 μm) was detected near the metal surface starting at 80 °C, and it became thicker (~25 μm) at higher temperatures (120 °C, 160 °C, and 200 °C). However, according to thermodynamic predictions (Pourbaix diagrams), as shown in Fig. 1, iron oxide should not be present in an aqueous H₂S environment since it is less stable than any of the various iron sulfides that can form. There it is seen that Fe₃O₄ is the most stable species in a pure H₂O-Fe system (see Fig. 1(a)), while iron sulfide is

more thermodynamically favored in the presence of aqueous H₂S (Fig. 1(b)). The red rectangular region represents the typical bulk pH and potential range seen in brines encountered in oil and gas transportation. While the bulk pH is often between 4 and 6, the pH at the steel surface, *i.e.*, the surface pH, is often approximately one unit higher than it is in the bulk [12], especially under low flow or in quiescent conditions. In the region of interest, at a high temperature, 120 °C for example, in a solution without H₂S, only Fe₃O₄ can form (Fig. 1(a)). With the addition of 0.1 bar H₂S, the Fe₃O₄ stability zone is completely replaced by a more thermodynamically favored mackinawite. In this graph, mackinawite is chosen as a meta-stable iron sulfide because it is most kinetically favored. However, other compounds such as pyrrhotite and pyrite can also be included in the analysis, as they are even more thermodynamic stable and would replace mackinawite. Pourbaix diagram determinations are based on bulk brine chemistry, *i.e.*, they can only predict the outer most thermodynamical stable corrosion product in contact with the bulk fluid. However, whether and what other corrosion product can form under the iron sulfide layer is still unknown, because the H₂S concentration underneath the iron sulfide layer can be much lower than that in the bulk solution. Indeed, iron oxide was clearly identified beneath the iron sulfide layer in a short-term (4 days exposure time) experimental study conducted by Gao, et al. [11]. Therefore, further research was warranted to investigate whether the unexpected iron oxide layer would keep growing or, as thermodynamics predicts, it is eventually converted into iron sulfide as the exposure time increases (research question #1).

The growth and phase transitions of polymorphous iron sulfides, with different stoichiometric ratios and structures, are complex. Direct observations are difficult to perform as some of these phases are

* Corresponding author.

E-mail address: sg389813@ohio.edu (S. Gao).

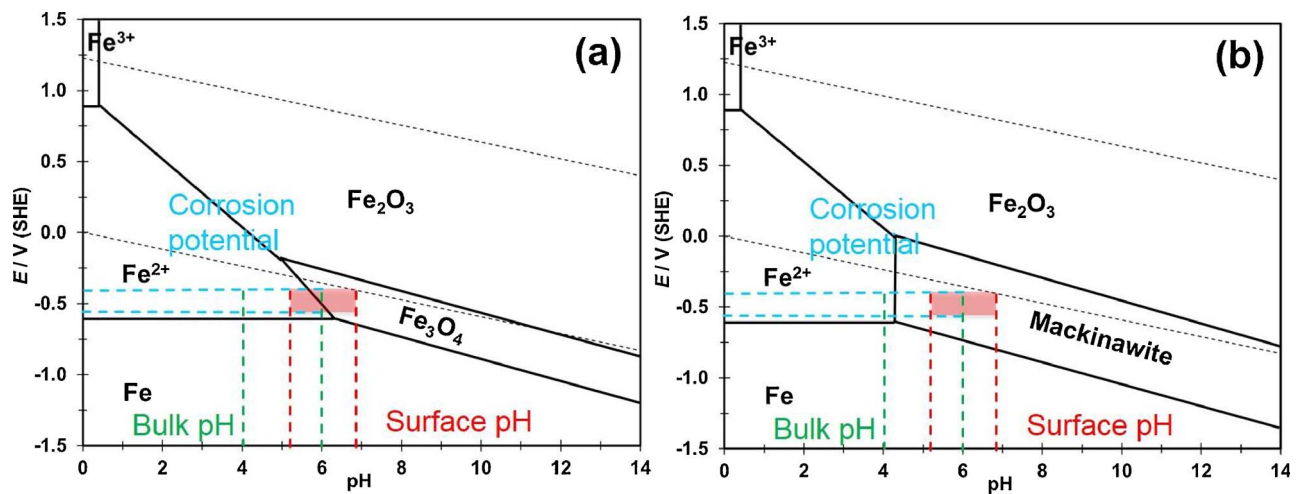


Fig. 1. Pourbaix diagrams for (a) H_2O -Fe system, (b) H_2S - H_2O -Fe system (only mackinawite is considered), $T = 120^\circ\text{C}$, $p_{\text{H}_2\text{S}} = 0.1$ bar.

Table 1
Iron sulfides typically encountered in H_2S corrosion environment [8].

Name	Formula	Crystal Structure	Properties
Mackinawite	FeS	Tetragonal; stacked layers of “2D” FeS sheets	Metastable, primarily precipitates from aqueous solution, initial corrosion product.
Cubic FeS	FeS	Cubic	Unstable, transforms into mackinawite, troilite or pyrrhotite. Does not form in the presence of oxygen or chlorides.
Troilite	FeS	Hexagonal	Stoichiometric member of the Fe_{1-x}S group ($x = 0$). Needle-like, flower-like, and beam-shaped morphologies.
Pyrrhotite	Fe_{1-x}S ($x = 0 \sim 0.17$)	Hexagonal $\text{Fe}_{10}\text{S}_{11}$, Monoclinic Fe_7S_8 or Orthorhombic	With vacancies, p-type semiconductor. Can co-exist with troilite, both are thermodynamically stable.
Greigite	Fe_3S_4	Cubic	Metastable $\text{Fe}^{\text{II}}\text{Fe}^{\text{III}}$ sulfide, associated with fresh water system.
Pyrite	FeS_2	Cubic	Stable iron(II) disulfide, cubic and framboidal (and raspberry-like) morphologies. Pyrite and pyrrhotite are the most stable iron sulfides.

unstable in certain environments and act as transition states. The typical iron sulfide encountered in H_2S corrosion environment are given in Table 1. Transformations among iron sulfides at 21°C were summarized by Shoosmith, et al. [13]. At low temperature, the reported sequence of the reaction products with time is mackinawite \rightarrow cubic FeS \rightarrow troilite \rightarrow pyrrhotite \rightarrow greigite (transition state) \rightarrow pyrite [14]. Bai, et al., [15] stated that troilite was the final corrosion product at 50°C after 96 h exposure time, but also found greigite and pyrite after 21 h under the same conditions [16]. This is somewhat contradictory to Shoosmith’s findings. The most likely reason are the different experimental conditions such as pH and $p_{\text{H}_2\text{S}}$ are often not well controlled or even properly defined during the tests, which makes the results difficult to reproduce. Considering that the formation/transformation and properties of iron sulfides are highly dependent on water chemistry, controlling the operating parameters is of prime importance. This problem can be addressed by first developing a comprehensive water chemistry prediction model [11] that can be used to calculate the desired operating conditions at any given temperature and then by closely monitoring those conditions. At elevated temperatures ($> 80^\circ\text{C}$), no work has yet been reported on the transformation sequence of iron sulfide (research question #2). In addition, the high temperature is fully expected to have a significant effect on the transformation kinetics.

As it pertains to the corrosion of steel, the protectiveness of iron sulfide layers is generally governed by pH, temperature, $p_{\text{H}_2\text{S}}$, time, and brine chemistry. Sardisco, et al., [17] found that the protectiveness of the sulfide layer changed at different pH values. Between pH 6.5–8.8, mackinawite was the least protective layer, compared to troilite and pyrite. Ren, et al., [18] observed that when the partial pressure of H_2S increased, fine grains of pyrrhotite formed that made the layer more compact and continuous, leading to a decrease of the general corrosion rate and a lower pitting tendency. Ning, et al., [19] have found that the

appearance of pyrite can initiate and sustain localized corrosion on steel. In summary, little is known about the protectiveness of the various iron sulfide polymorphs found in the corrosion product layer at high temperature (research question #3).

In order to address the three research questions stated above, H_2S corrosion tests were performed on carbon steel at 120°C with exposure times of 1, 4, 7, and 21 days. X-ray diffraction (XRD), scanning electron microscopy with energy dispersive X-ray spectroscopy microanalysis (SEM/EDS), and linear polarization resistance (LPR) methods were employed to investigate the time-dependent formation of iron oxide, the transformation of iron sulfide polymorphs, and consequently, their roles in corrosion at elevated temperature. The corrosion product layer was also characterized by selected area diffraction (SAD) measurements, conducted in conjunction with transmission electron microscopy (TEM).

2. Experimental procedure

Experiments were conducted in a 7 L autoclave made from Hastelloy C276, shown in Fig. 2. A conventional three-electrode setup was used to conduct LPR measurements. The working electrode was a cylindrical API 5L X65 carbon steel sample. The chemical composition of this ferritic-pearlitic steel is shown in Table 2. A Pt-coated Nb cylinder was used as the counter electrode and a commercial Zr/ZrO₂ high temperature, high pressure pH probe was used as a pseudo reference electrode. While the exact potential was still unknown, this pseudo reference electrode served its purpose as long as its potential was stable under the operating conditions [11]. Additional flat samples were also suspended using a PTFE-coated 304 stainless steel wire. A centrally mounted impeller on a rotating shaft was used to keep the solution well mixed during each experiment.

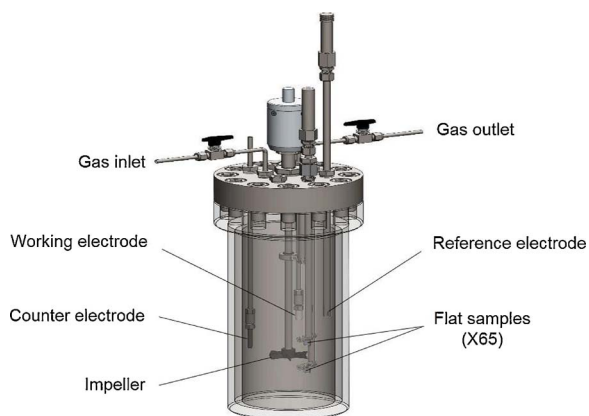


Fig. 2. Experimental 7 L Hastelloy autoclave setup.

Table 2
Chemical composition of API 5L X65 carbon steel (wt.%).

Cr	Mo	S	V	Si	C	P	Ni	Mn	Fe
0.14	0.16	0.009	0.047	0.26	0.13	0.009	0.36	1.16	Balance

Table 3
Test matrix for the effect of time.

Parameter	Value
Temperature	120 °C
pH ₂ S	0.10 bar
Total pressure	8.92 bar
Initial pH at 120 °C	4.0
[H ₂ S] _{aq}	0.00385 mol/L
Rotating speed	1000 rpm
Duration	1, 4, 7, and 21 day(s)

To be able to reach the desired experimental conditions at high temperature (summarized in Table 3), the corresponding initial conditions in the autoclave at room temperature were defined based on calculations performed using an in-house water chemistry model [11]. The temperature was selected to be 120 °C to avoid the rapid formation of pyrite. Pyrite was expected to form at higher temperatures and causes severe localized attack [20], which would greatly affect the experimental results. The testing electrolyte was 1 wt% NaCl.

The following experimental procedures were executed repeatedly on all of the experiments. Before each experiment, the mild steel specimen was polished with 400 and 600 grit sandpaper, then rinsed with deionized water and isopropanol. The solution was sparged with N₂ gas overnight to remove oxygen. Then the pH at room temperature was

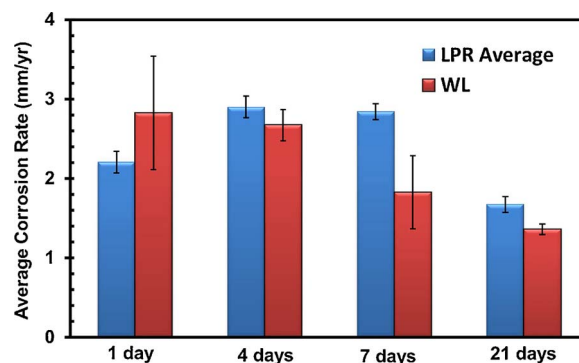


Fig. 4. Comparison of average corrosion rates between the integrated average of LPR measurements and weight loss, T = 120 °C, pH₂S = 0.10 bar, initial pH = 4.0, B = 23 mV/decade.

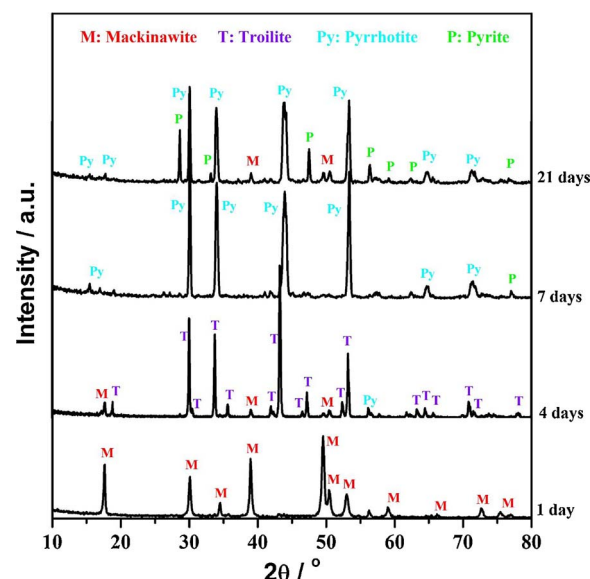


Fig. 5. XRD patterns of corrosion products on the steel surface for different test durations, T = 120 °C, pH₂S = 0.10 bar, initial pH = 4.0.

adjusted according to the water chemistry calculations to achieve an initial pH of 4.0 when the temperature reached 120 °C. The next steps were to rapidly pressurize the autoclave with an H₂S/N₂ gas mixture to achieve an initial 0.10 bar partial pressure of H₂S at 120 °C and to turn on the autoclave heater.

After reaching the desired temperature (in less than 30 min), LPR was conducted by polarizing the steel ± 5 mV from the open circuit

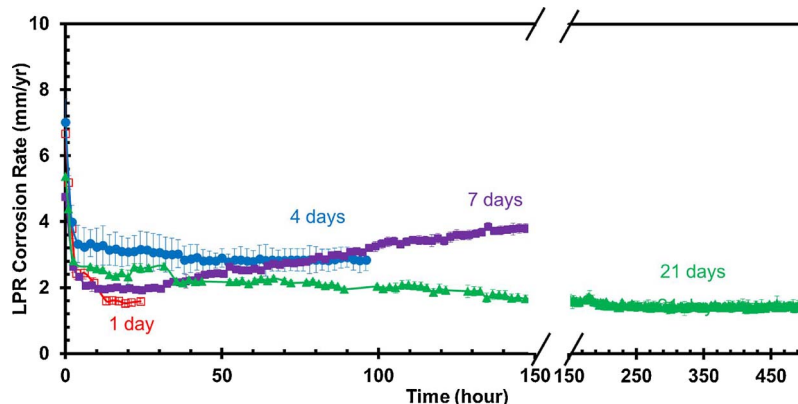


Fig. 3. Corrosion rate for different test durations from LPR measurements, T = 120 °C, pH₂S = 0.10 bar, initial pH = 4.0, B = 23 mV/decade.

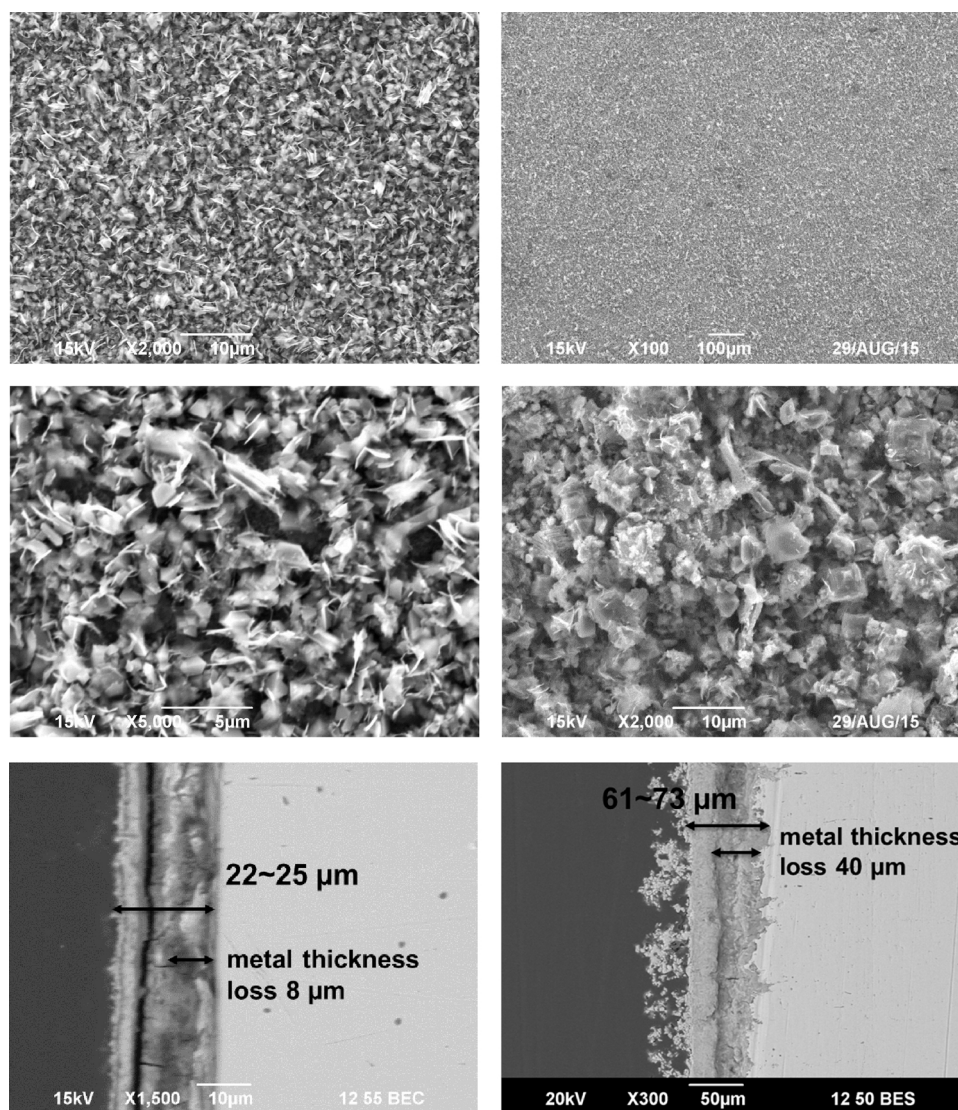


Fig. 6. SEM morphologies and cross sections for 1 day (left) and 4 days (right), $T = 120\text{ }^{\circ}\text{C}$, $\text{pH}_2\text{S} = 0.10\text{ bar}$, initial $\text{pH} = 4.0$.

potential (OCP) at a scanning rate of 0.125 mV/s . LPR corrosion rate data was collected approximately every 2 h during the experiments. The slope of the LPR line corresponds to the polarization resistance R_p . The solution resistance R_s can be obtained from EIS (electrochemical impedance spectroscopy) measurement. Then the corrosion current (A/m^2) can be calculated as:

$$i_{\text{corr}} = \frac{B}{R_p - R_s} \quad (1)$$

The corrosion current was converted to corrosion rate by using the following equation [21]:

$$CR = \frac{M_w i_{\text{corr}}}{nF\rho A} \quad (2)$$

where M_w is molecular weight (55.8 g/mol), n is the number of electron transferred, F is Faraday constant, ρ the density of iron (7.87 g/cm^3), A the electrode area in cm^2 . Then the average LPR corrosion rate was compared with the weight loss (WL) corrosion rate and the B value was optimized.

At the conclusion of each experiment, the solution in the autoclave was cooled to approximately $50\text{ }^{\circ}\text{C}$ and the H_2S concentration and Fe^{2+} concentration were measured by using micro gas chromatography (GC) and spectrophotometry, respectively. The corroded specimens were

retrieved, dehydrated and stored in a desiccator. The corrosion product layer was analyzed by using XRD, for composition, and morphologically characterized by SEM. To identify the inner iron oxide layer, FIB sample preparation was followed by SAD, performed in conjunction with TEM. After removing the corrosion products from the specimen, the steel surface was examined by optical surface profilometry. Other experimental details can be found elsewhere [11].

3. Results and discussion

3.1. Corrosion rates

Fig. 3 shows the corrosion rates measured by using LPR for nominally identical conditions and different test durations: 1, 4, 7, and 21 days. For all experiments, the initial corrosion rate was around 6 mm/yr , which then decreased rapidly in the first day and stabilized between 2 and 4 mm/yr . Although initial conditions were well controlled, once the autoclave had been closed, there was no control of the operating parameters other than temperature and total pressure. Therefore, it is difficult to know how the water chemistry in the autoclave exactly evolved (pH , H_2S concentration, etc.). It has mostly likely diverged in different experiments leading to some scatter between the experimental results. All four repeats show very similar behavior on the

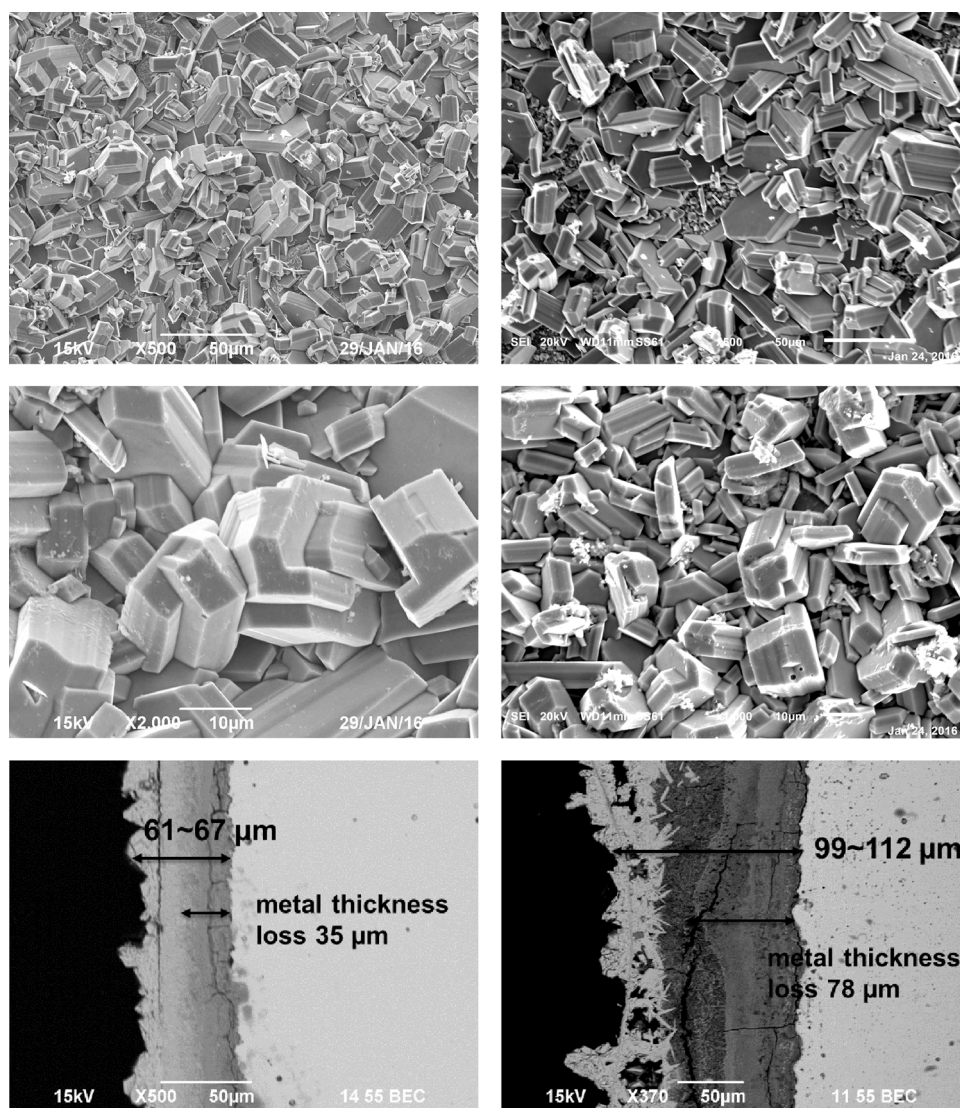


Fig. 7. SEM morphologies and cross sections for 7 days (left) and 21 days (right), $T = 120\text{ }^{\circ}\text{C}$, $\text{pH}_2\text{S} = 0.10\text{ bar}$, initial $\text{pH} = 4.0$.

Table 4
Summary of the theoretical calculated final conditions at $120\text{ }^{\circ}\text{C}$.

Duration, day(s)	Final Conditions		
	pH_2S , bar	pH	Fe^{2+} , ppm
1	0.09	5.7	7.4
4	0.11	5.5	5.8
7	0.09	5.6	5.1
21	0.09	5.5	4.2

first few days. In longer exposure the 7-day experiment showed an unexpected increase in the corrosion rate. However, this was only observed on the working electrode but not on the independent weight loss specimens.

In order to validate the corrosion rate measurements based on LPR data, the integrated area under the corrosion rate curves in Fig. 3 were compared to the measured WL values as shown in Fig. 4. The LPR calculations used a B value of 23 mV/decade to obtain the mean corrosion rate value, while the error bars reflect the variation in estimating the polarization resistance from the nonlinear current-voltage curves. For the WL specimens the error bars represent the maximum and minimum values obtained from the three samples exposed at the same time. It is important to point out that the high temperature

electrochemical measurements are inherently difficult to perform, especially in sour environments. Some unsatisfactory agreement between LPR and WL measurements is noticed in some conditions, especially in the 7 days exposure experiment. The WL corrosion rate is more reliable and preferred. In these conditions, the LPR corrosion rate only gives at best a trend and caution should be taken in interpreting the data.

3.2. Outer iron sulfide layer

The outer corrosion product layers on the steel surface were characterized by XRD. From Fig. 5, the corrosion product was identified as pure mackinawite (FeS) after 1 day of exposure. Most of the mackinawite changed to troilite (FeS) after 4 days of exposure. Troilite transformed to pyrrhotite (Fe_{1-x}S , $0 \leq x \leq 0.17$) with a trace amount of pyrite (FeS_2) after 7 days of exposure. After 21 days, more pyrite was observed in addition to pyrrhotite. With increasing time, the corrosion products had an increased sulfur content in their composition. Quantitative analysis of acquired XRD data indicates the proportion of pyrite was around 12% after 21 days.

The corrosion products and cross-sections were also characterized by SEM as shown in Fig. 6 and Fig. 7. An inner and an outer corrosion product layer are apparent in the cross-section analysis. The

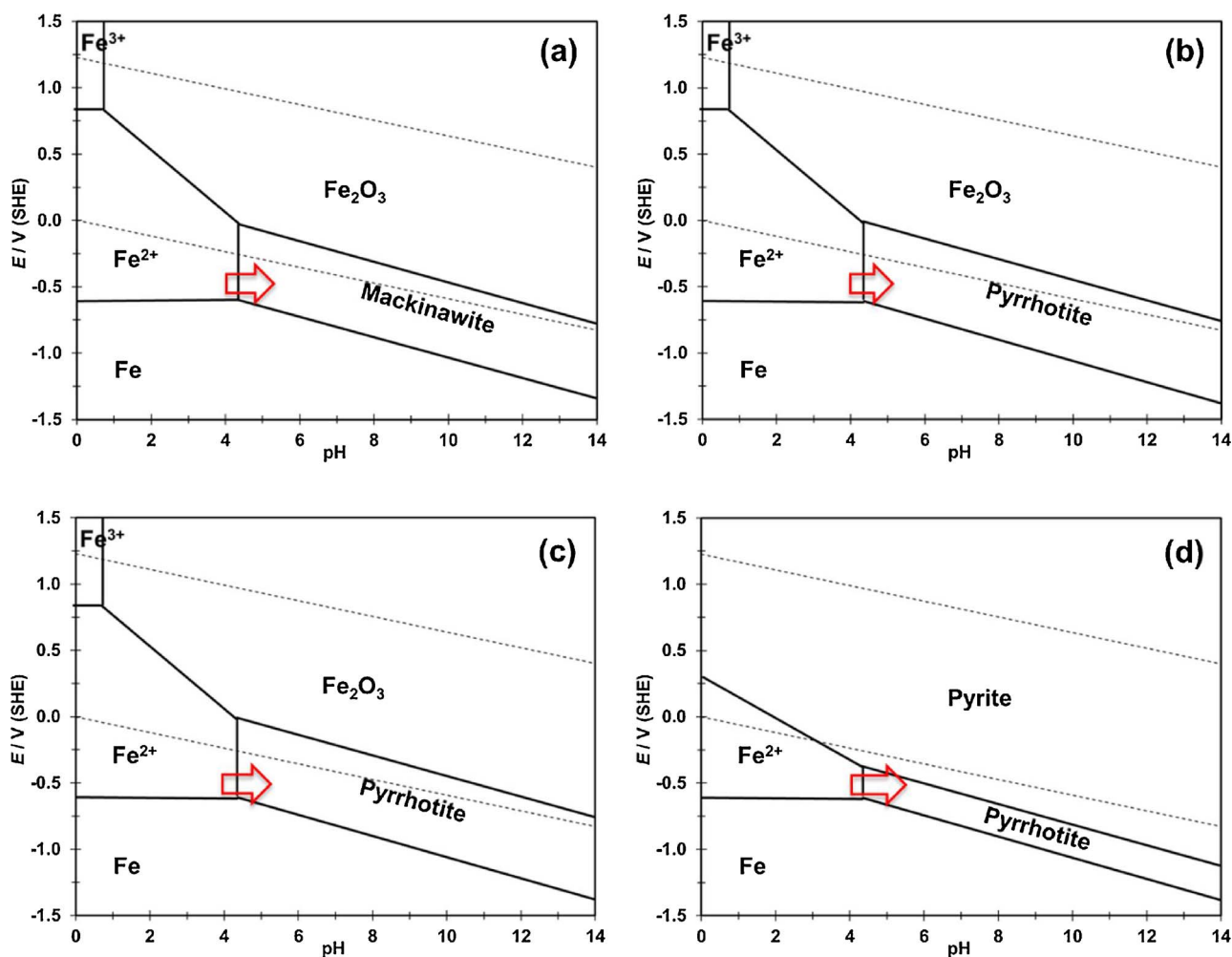


Fig. 8. Pourbaix diagrams for Fe-H₂S-H₂O system by considering (a) mackinawite, (b) pyrrhotite (troilite), (c) pyrrhotite, and (d) pyrite/pyrrhotite, T = 120 °C, other input parameters are in Table 4.

composition of the inner layer is discussed in the next section while the following paragraphs focus on the outer iron sulfide layer.

After 1 day of exposure, the SEM shows a typical flaky mackinawite [22] product layer approximately 22 μm in thickness. For comparison, the metal thickness losses (*l*) were also determined from WL:

$$l = \frac{WL}{\rho A} \quad (3)$$

Where *A* is the surface area of the weight loss specimen.

For the 4 day experiment, the SEM shows troilite particles on the surface and a much thicker layer (61 ~ 73 μm). Well-defined hexagonal pyrrhotite prisms appeared on the surface after 7 days. After 21 days of exposure, it can be seen that the crystal size increased with time as the corrosion product layer thickness grew above 100 μm. In summary, the transformation sequence of iron sulfide observed at high temperature was mackinawite (1 day) → troilite (4 days) → pyrrhotite (7 days) → pyrite (12%) and pyrrhotite (21 days), which is basically the same sequence as seen at low temperature, except that no cubic FeS or greigite was observed. Another difference that can be noted is that the corrosion products observed at low temperature are typically a mixture of more than three iron sulfides without a major phase [10,15,16], while a major phase was obvious at high temperature in this study. This infers that the observed transformation sequence appears more conclusive at high temperature.

The H₂S and Fe²⁺ concentrations were measured by using micro gas chromatography (GC) and spectrophotometry, respectively, after the solution in the autoclave was cooled to approximately 50 °C (following

a necessary safety-related procedure that took approximately 30 min). Assuming the dissolution and precipitation rates of iron sulfide are slow, the Fe²⁺ concentration at this sampling temperature (50 °C) was considered to be the same as at the experimental temperature (120 °C). Applying a molar balance for sulfur species, the pH and pH₂S can be calculated for the end of the experiment. The details of the calculation can be found in elsewhere [11].

The calculated parameters are summarized in Table 4 and used as the inputs to generate Pourbaix diagrams, as shown in Fig. 8. The vertical position and the width of the arrow in each diagram represent the potential in the final stages of the experiments (which varied between approximately -550 mV vs. SHE). The length of the arrow represents the pH drift experienced during the test from initial pH 4.0 to the final pH 5.5–5.7, as shown in Table 4. For the 1-day experiment, only mackinawite was considered for the Pourbaix diagram since it always forms as the initial iron sulfide layer, due to a fast kinetics [22]. For the 4-day and 7-day experiment, both mackinawite and pyrrhotite were considered in the construction of the diagram (troilite is the ending member of pyrrhotite (Fe_{1-x}S) when *x* is zero). Mackinawite, pyrrhotite, and pyrite were all included in the analysis for long-term exposure (21 days). It can be seen that all the arrows cross over into the stability regions for different iron sulfides, as identified by the XRD. Particularly, the tip of the arrow, which represents the final experimental conditions, is very close to the equilibrium line between pyrrhotite and pyrite for 21-day experiment. This suggests the transformation reaction between pyrrhotite and pyrite. The experimental XRD results are in good qualitative agreement with the thermodynamic

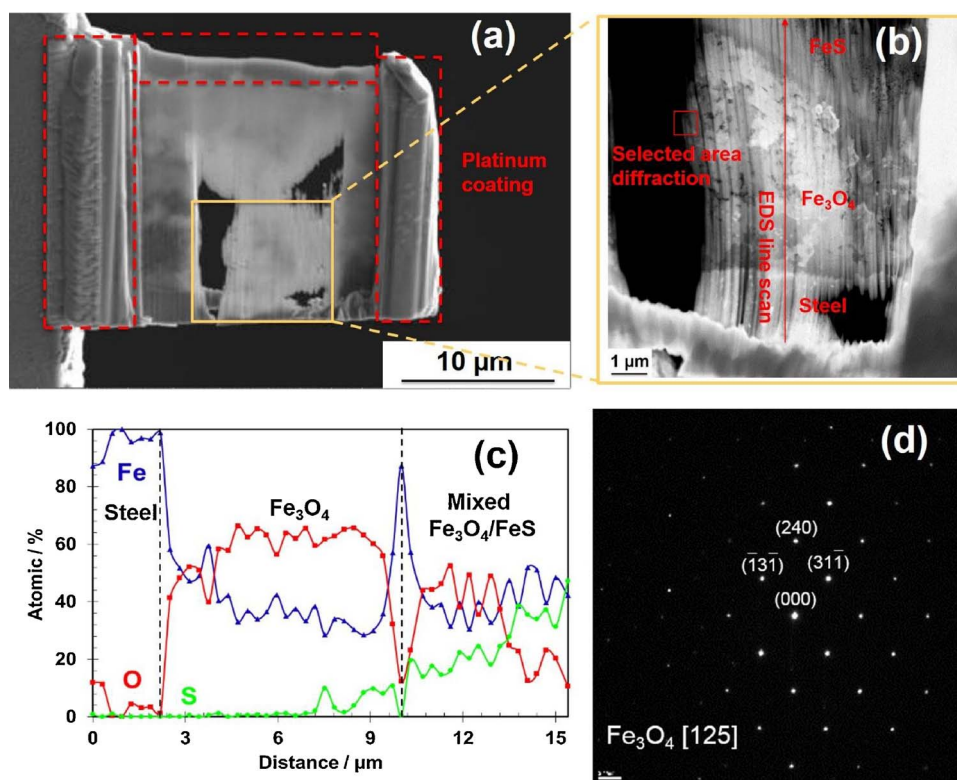


Fig. 9. (a) FIB sample preparation; (b) thin area for TEM analysis; (c) EDS line scan result; (d) selected area diffraction (SAD) pattern. $T = 120\text{ }^{\circ}\text{C}$, $\text{pH}_2\text{S} = 0.20\text{ bar}$, initial $\text{pH} = 4.0$, 4 days.

calculations. With the increase of time, metastable mackinawite transformed to thermodynamically more stable iron sulfide phases such as troilite, pyrrhotite, and pyrite [23].

3.3. Inner iron oxide layer

SEM analysis of specimen cross-sections suggests the presence of a different inner layer, expected to be comprised of iron oxide [11], which could not be detected by XRD (Fig. 5), warranting further analysis, because the outer corrosion product layer was too thick and/or too compact so that the X-rays could not penetrate and detect the layers underneath. Therefore, focused ion beam combined with transmission electron microscopy (FIB/TEM) analysis was conducted to address this issue and to characterize this inner layer. The methodology involves the sectioning of a very thin slice of material around the steel/corrosion product layer using a FIB, with subsequent microscopic and elemental analysis using TEM/EDS. Fig. 9(a) shows the sample prepared by FIB. The surfaces of the slice were coated with platinum to prevent it from collapsing since it is extremely thin. The area marked by a yellow rectangle was further thinned and analyzed by TEM. As shown in Fig. 9(b), it is apparent that there are two interfaces, indicating the existence of multiple layers. The EDS line scan from left to right in Fig. 9(c) corresponds to the vertical arrow shown in Fig. 9(b). EDS line scan analysis initially only detects Fe, which corresponds to the steel matrix. Above the steel matrix, both Fe and O were detected, demonstrating the inner layer was comprised of an iron oxide layer. Starting at the interface between the inner and outer layers, increasing amount of S and decreasing amount of O were detected as the scan progresses through the outermost layer, meaning that the outer layer was made of a mixture of iron oxide and FeS. From the EDS analysis, it is expected that the brine side of the outer layer will be entirely made of FeS, which is confirmed by XRD analysis. The XRD focuses on the outer most iron sulfide layer (5–10 μm), while the EDS analysis here only examined the initial a few microns of the inner most iron sulfide layer. A selected area

diffraction (SAD) pattern collected from the iron oxide layer (Fig. 9(b)) identified the Fe_3O_4 (125) plane (Fig. 9(d)). This is an important discovery since Fe_3O_4 can be very protective and greatly slow down the corrosion rate at high temperature, as was confirmed in previous studies of aqueous corrosion at elevated temperatures in CO_2 environments [24].

In addition to identifying the composition of the corrosion product layer, one of the objectives of this study was to investigate if the thermodynamically less stable Fe_3O_4 layer would vanish over time by converting into more stable species. Fig. 10 shows the EDS mapping results of the specimen cross-sections for different experiment durations. The color in each image qualitatively indicates the elemental composition of each layer (with dark blue and pink represent low and high content, respectively). After the 1 day experiment, the inner Fe_3O_4 layer was about 20 μm thick while the outer mackinawite layer was only several μm . Specimen removed from other experiments (1 day, 7 days & 21 days) indicate the iron sulfide layer grew thicker over time. From Fig. 10, the magnetite and iron sulfide layer thickness was estimated from the EDS maps and shown in the graph presented in Fig. 11.

Interestingly, the thickness of Fe_3O_4 remained almost constant at around 25 μm . It did not vanish over time although it is thermodynamically less stable than iron sulfide. The thickness of iron sulfide layer gradually grew from a few micrometers up to 70 μm . The Pourbaix diagrams shown in Fig. 8 only predict thermodynamically stable corrosion product layers based on bulk conditions. This corresponds mostly to the outer iron sulfide layer. The presence of Fe_3O_4 close to the steel substrate cannot be predicted by the Pourbaix diagram because the surface conditions could be very different from the bulk. It is also postulated that H_2S is consumed within the FeS layer and is not in direct contact with Fe_3O_4 (except at the $\text{Fe}_3\text{O}_4/\text{FeS}$ interface), which means that the electrolyte trapped in the porous Fe_3O_4 layer is free of sulfide species and constitutes, with the steel, an 'Fe- H_2O ' system rather than an 'Fe- H_2S - H_2O ' system.

In this environment, the formation of Fe_3O_4 is explained by the iron

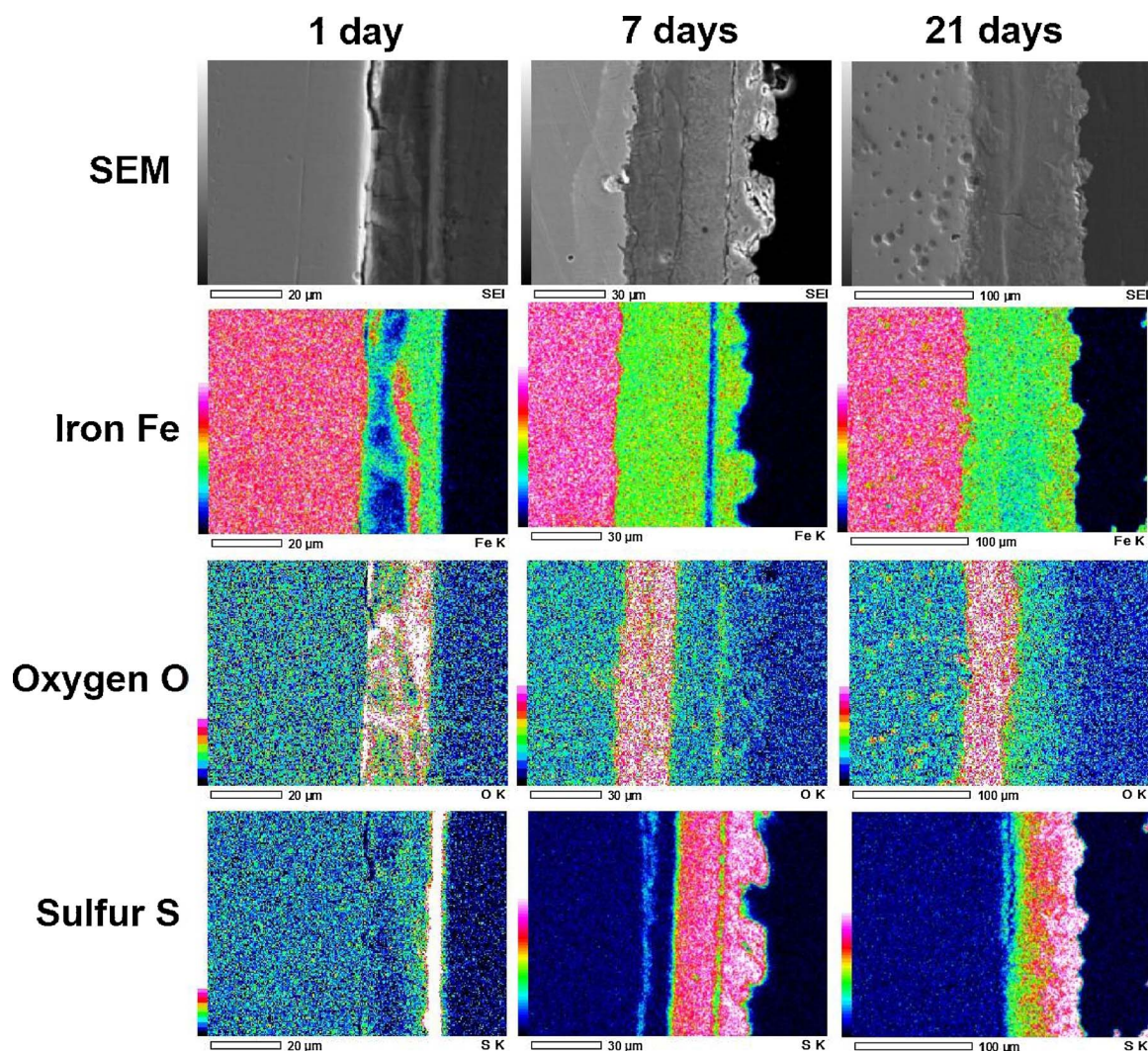


Fig. 10. EDS mapping results for Fe, O and S distribution for different experiment durations, $T = 120\text{ }^{\circ}\text{C}$, $\text{pH}_2\text{S} = 0.10\text{ bar}$, initial $\text{pH} = 4.0$.

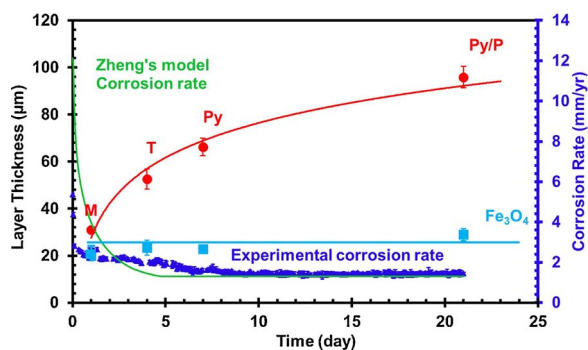


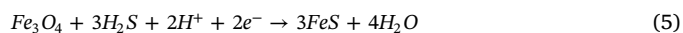
Fig. 11. Layer thickness of Fe_3O_4 and iron sulfides after different exposure time, and compared with the LPR corrosion rates from experimental data and Zheng's model [7], M: mackinawite, T: troilite, Py: pyrrhotite, P: pyrite, $T = 120\text{ }^{\circ}\text{C}$, $\text{pH}_2\text{S} = 0.10\text{ bar}$, initial $\text{pH} = 4.0$.

dissolution and the release of Fe^{2+} ions which react with the surrounding H_2O molecules to form Fe_3O_4 via reaction (4) [24]:



Kinetically, it seems there is a competition between Fe_3O_4 and iron sulfide formation. At day 1, the Fe_3O_4 layer is much thicker than the FeS layer. However, the iron sulfide layer appears to continuously grow while the Fe_3O_4 layer thickness remains constant. This observation

suggests a process involving continuous Fe_3O_4 formation due to corrosion at the steel/ Fe_3O_4 interface, and Fe_3O_4 conversion to FeS at the Fe_3O_4 /FeS interface via reaction (5) [25]:



Conversely, the FeS layer grows both by conversion from Fe_3O_4 and also by precipitation as the Fe^{2+} ions can diffuse through the Fe_3O_4 layer and react with $\text{H}_2\text{S}/\text{HS}^-$ inside the FeS layer.

In addition, the experimentally measured corrosion rate decreased quickly in the first days when only magnetite and mackinawite formed. However, whether this decrease was due to magnetite or mackinawite formation remains uncertain. This became the subject of further investigations [25].

The results reported herein were compared with results of calculations done with the recent H_2S corrosion model developed by Zheng, et al. [9], developed for by using low temperature data ($< 80\text{ }^{\circ}\text{C}$). It should be stated that Zheng's model is a uniform corrosion model and only considers mackinawite as the iron sulfide layer. Consequently, it is unsurprising that the initial corrosion rate is overestimated since the model does not take into account the presence of a magnetite layer. The final stable corrosion rate for LPR measurements and Zheng's model are in much better agreement, which is encouraging. Severe localized corrosion experienced with the formation of pyrite in long term exposures, must have influenced the LPR measurements [11] and this phenomenon cannot be captured by Zheng's model. The present study

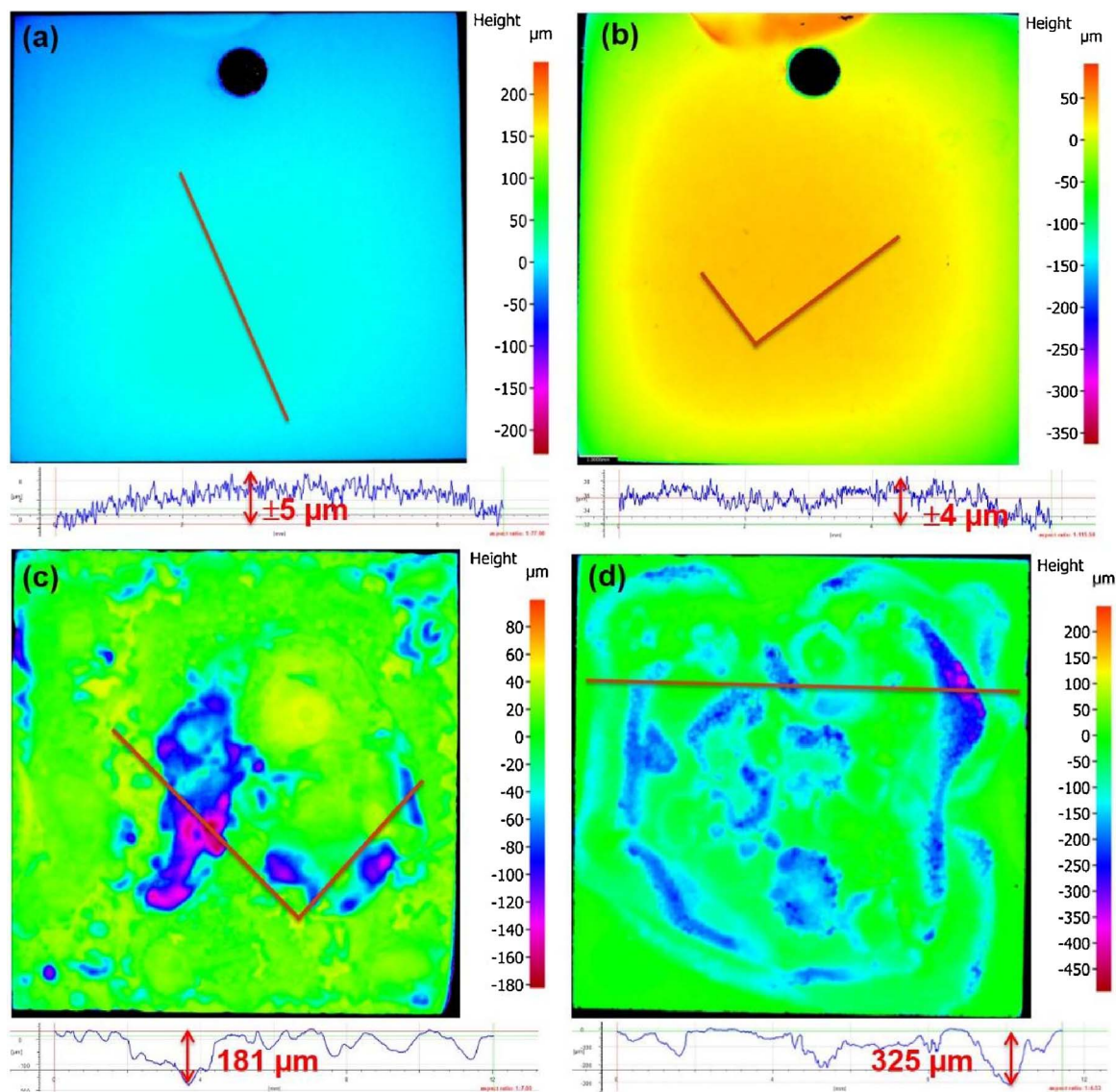


Fig. 12. Surface profilometry after removing corrosion products (a) 1 day, mackinawite; (b) 4 days, troilite; (c) 7 days, pyrrhotite/pyrite; (d) 21 days, pyrrhotite/pyrite. $T = 120\text{ }^{\circ}\text{C}$, $\text{pH}_2\text{S} = 0.10\text{ bar}$, initial $\text{pH} = 4.0$.

highlights several gaps in the modeling approach, which should, nevertheless, be used as a good starting point building a model for prediction of H_2S corrosion at high temperature.

3.4. Surface profilometry

After removal of both the inner and outer corrosion products using Clarke solution [26], the metal surface was characterized by profilometry, as shown in Fig. 12. No obvious localized corrosion was observed after 1 day and 4 days. The surface was relatively smooth. In the presence of mackinawite and troilite, which were the phases identified in these conditions, the corrosion attack could be considered to be uniform. However after 7 days of exposure, when pyrrhotite and a small amount of pyrite formed, localized corrosion was observed with a pit depth of $181\text{ }\mu\text{m}$, which amounts to a time averaged pit penetration rate of 9.4 mm/yr and a 5.2 pitting ratio (pit penetration rate over uniform corrosion rate). After 21 days exposure time, with more pyrite formation, the localized corrosion progressed further. Some pits were as deep as $325\text{ }\mu\text{m}$, corresponding to a time averaged pit penetration rate of 5.6 mm/yr and a 4.3 pitting ratio. The results are consistent with previous suggestions [19] that link the presence of pyrite to localized

corrosion.

Fe_3O_4 formed at high temperature in CO_2 environment is considered protective against both uniform and localized corrosion [27]. However, there is very few reliable high temperature experimental data available for H_2S environments. It has been reported that any disruption leading to a discontinuity in the FeS layer could result in initiation of localized corrosion. The discontinuity or inhomogeneity in the layer can result from mechanical damage, poor adhesion to the steel surface or transformation to other sulfide phases or polymorphs. The localized corrosion then precedes due to the galvanic effect between the underlying steel and the conductive iron sulfide layers [28]. In the current study, the disruptions were most likely caused by crystallographic dimensions changes from different iron sulphides (monoclinic for pyrrhotite to cubic for pyrite, for example) leading to differences in electrical conductivity. Moreover, Fe_3O_4 has been reported to be a very good electrical conductor [29], which means the galvanic effect between the steel and iron sulfide layer was not impaired by Fe_3O_4 and consequently the localized corrosion still occurs.

4. Conclusions

The formation of iron oxide (Fe_3O_4) and iron sulfide, and their effects on corrosion, were investigated in a high temperature aqueous H_2S environment. The main conclusions are summarized below:

1. Fe_3O_4 formation at high temperature

Fe_3O_4 always formed as the inner layer due to corrosion, although it was thermodynamically less stable than iron sulfide. Fe_3O_4 was still detected even after long exposures as it is kinetically favored in the conditions used here. The Fe_3O_4 layer thickness did not change with time, which could infer a continuous process of Fe_3O_4 formation by corrosion and a conversion to mackinawite at approximately the same rate. A model for high temperature corrosion of mild steel in aqueous H_2S environment at high temperature should include Fe_3O_4 formation.

2. Iron sulfide formation and transformation at high temperature

The observed transformation sequence for iron sulfides under these conditions was mackinawite (1 day) \rightarrow troilite (4 days) \rightarrow pyrrhotite (7 days) \rightarrow pyrite (12%)/pyrrhotite (21 days). The thickness of iron sulfide layer increased with time.

3. Role of layers in corrosion at high temperature

The general corrosion rate rapidly decreased (from approximately 6 mm/yr to 2 mm/yr) on the first day with the formation of Fe_3O_4 and mackinawite. Both of these corrosion products are known to retard the general corrosion rate, and the question remains open on which is dominant. The general corrosion rate (~ 2 mm/yr) remained steady as mackinawite converted to troilite and pyrrhotite. When pyrite formed, severe localized corrosion was observed.

Acknowledgements

The authors would like to thank Dr. Srdjan Netic for his comments, advice and help in preparing this manuscript, and the following industrial sponsors for their financial support and direction: Anadarko, Baker Hughes, BP, Chevron, China National Offshore Oil Corporation, CNPC Tubular Goods Research Center, ConocoPhillips, DNV GL, ExxonMobil, M-I SWACO, Occidental Oil Company, Petroleum Institute, PTT, Saudi Aramco, Shell Global Solutions, SINOPEC, TOTAL, TransCanada, WGK.

References

- [1] G. DeBruijn, High-pressure, high-temperature technologies, *Oilfield Rev.* 20 (2008) 46–60.
- [2] X.H. Zhao, Y. Han, Z.Q. Bai, B. Wei, The experiment research of corrosion behaviour about Ni based alloys in simulant solution containing $\text{H}_2\text{S}/\text{CO}_2$, *Electrochim. Acta* 56 (2011) 7725–7731.
- [3] A. Shadravan, M. Amani, HPHT 101-what petroleum engineers and geoscientists should know about high pressure high temperature wells environment, *Energy Sci. Technol.* 4 (2012) 36–60.
- [4] S. Gao, C. Dong, A. Fu, K. Xiao, X. Li, Corrosion behavior of the expandable tubular in formation water, *Int. J. Min. Metall. Mater.* 22 (2015) 149–156.
- [5] H. Mansoori, R. Mirzaee, F. Esmaeilzadeh, A. Vojood, A. Dowran, Pitting corrosion failure analysis of a wet gas pipeline, *Eng. Fail. Anal.* 82 (2017) 16–25.
- [6] A. Zhong, Challenges for high-pressure high-temperature applications of rubber materials in the oil and gas industry, *Residual Stress, Thermomechanics & Infrared Imaging, Hybrid Techniques and Inverse Problems* 9 Springer, 2016.
- [7] W.D. Grimes, R.I. McNeil, Prediction of Hydrogen Sulfide and Carbon Dioxide in HPHT Wells, *SPE HPHT Advanced Technology Symposium*, Woodlands, TX, USA, (2005) (Paper No. SPE 97568).
- [8] J. Ning, Y. Zheng, D. Young, B. Brown, S. Netic, Thermodynamic study of hydrogen sulfide corrosion of mild steel, *Corrosion* 70 (2014) 375–389.
- [9] Y. Zheng, J. Ning, B. Brown, S. Netic, Advancement in predictive modeling of mild steel corrosion in CO_2 - and H_2S -containing environments, *Corrosion* 72 (2016) 679–691.
- [10] F. Shi, L. Zhang, J. Yang, M. Lu, J. Ding, H. Li, Polymorphous FeS corrosion products of pipeline steel under highly sour conditions, *Corros. Sci.* 102 (2016) 103–113.
- [11] S. Gao, P. Jin, B. Brown, D. Young, S. Netic, M. Singer, Corrosion behavior of mild steel in sour environments at elevated temperatures, *Corrosion* 73 (2017) 915–926.
- [12] J. Han, B. Brown, D. Young, S. Netic, Mesh-capped probe design for direct pH measurements at an actively corroding metal surface, *J. Appl. Electrochem.* 40 (2010) 683–690.
- [13] D.W. Shoesmith, P. Taylor, M.G. Bailey, D.G. Owen, The formation of ferrous monosulfide polymorphs during the corrosion of iron by aqueous hydrogen sulfide at 21 °C, *J. Electrochem. Soc.* 125 (1980) 1007–1015.
- [14] J.B. Sardisco, R.E. Pitts, Corrosion of Iron in an H_2S - CO_2 - H_2O system composition and protectiveness of the sulfide film as a function of pH, *Corrosion* 21 (1965) 350–354.
- [15] P. Bai, S. Zheng, H. Zhao, Y. Ding, J. Wu, C. Chen, Investigations of the diverse corrosion products on steel in a hydrogen sulfide environment, *Corros. Sci.* 87 (2014) 397–406.
- [16] P. Bai, S. Zheng, C. Chen, H. Zhao, Investigation of the iron-sulfide phase transformation in nanoscale, *Cryst. Growth Des.* 14 (2014) 4295–4302.
- [17] J.B. Sardisco, R.E. Pitts, Corrosion of iron in an H_2S - CO_2 - H_2O system composition and protectiveness of the sulfide film as a function of pH, *Corrosion* 21 (1965) 350–354.
- [18] C. Ren, D. Liu, Z. Bai, T. Li, Corrosion behavior of oil tube steel in simulant solution with hydrogen sulfide and carbon dioxide, *Mater. Chem. Phys.* 93 (2005) 305–309.
- [19] J. Ning, Y. Zheng, B. Brown, D. Young, S. Netic, The role of iron sulfide polymorphism in localized H_2S corrosion of mild steel, *Corrosion* 73 (2017) 155–168.
- [20] S. Gao, P. Jin, B. Brown, D. Young, S. Netic, M. Singer, Effect of high temperature on the aqueous H_2S corrosion of mild steel, *Corrosion* 73 (2017) 1188–1191.
- [21] J.R. Scully, Polarization resistance method for determination of instantaneous corrosion rates, *Corrosion* 56 (2000) 199–218.
- [22] J. Ning, Y. Zheng, B. Brown, D. Young, S. Netic, A thermodynamic model for the prediction of mild steel corrosion products in an aqueous hydrogen sulfide environment, *Corrosion* 71 (2015) 945–960.
- [23] D. Rickard, G.W. Luther, Chemistry of iron sulfides, *Chem. Rev.* 107 (2007) 514–562.
- [24] T. Tanupabrunsun, B. Brown, S. Netic, Effect of pH on CO_2 Corrosion of Mild Steel at Elevated Temperatures, *NACE, Orlando, FL USA, 2013 (Corrosion/2013, Paper No. 2348)*.
- [25] S. Gao, B. Brown, D. Young, S. Netic, M. Singer, Formation Mechanisms of Iron Oxide and Iron Sulfide at High Temperature in H_2S Corrosion Environment, *NACE, Phoenix, AZ USA, 2018 (Corrosion/2018, Paper No. 11027)*.
- [26] D. Singh, A. Kumar, A fresh look at ASTM G 1-90 solution recommended for cleaning of corrosion products formed on iron and steels, *Corrosion* 59 (2003) 1029–1036.
- [27] B. Mishra, S. Al-Hassan, D.L. Olson, M.M. Salama, Development of a predictive model for activation-controlled corrosion of steel in solutions containing carbon dioxide, *Corrosion* 53 (1997) 852–859.
- [28] S.N. Esmaeely, G. Bota, B. Brown, S. Netic, Influence of pyrrhotite on the corrosion of mild steel, *Corrosion* 74 (2018) 37–49.
- [29] R. Prakash, R.J. Choudhary, L.S.S. Chandra, N. Lakshmi, D.M. Phase, Electrical and magnetic transport properties of Fe_3O_4 thin films on GaAs (100) substrate, *J. Phys. Condens. Matter* 19 (2007) 1–21.